PNAS RESEARCH ARTICLE | MICROBIOLOGY OPEN ACCESS

Intercalated bacterial biofilms are intrinsic internal components of calcium-based kidney stones

William C. Schmidt[a,b,c,d,1], Ava Mousavi[e,1], Jiahui Li[f], Rena Yang[a,b,c,d], Gerson Gonzalez Marin[g], Henry L. Schreiber IV[h,i], Rachael E. S. Hammann[h,i], Chloe L. P. Obernuefemann[h,i], Karla Bergeron[j], Aleksandra Klim[j], Daniel Wong[j], Kefu Du[j], Scott J. Hultgren[h,i], Qian Chen[f,k,l,m], Aaron Celestian[g], Gerard C. L. Wong[a,b,c,d,2], and Kymora B. Scotland[e,2]

Affiliations are included on p. 10.

Edited by Joanna Aizenberg, Harvard University, Allston, MA; received July 2, 2025; accepted December 15, 2025

Calcium oxalate stones comprise greater than 70% of all kidney stones. In the current conceptual framework, the initial stone nidus is thought to include the aggregation of inorganic crystallites, the formation of which is favored by elevated concentrations of dissolved constituents. Here, we show that this highly prevalent stone type comprises a form of organic–inorganic polycrystalline biocomposite with integrated bacterial biofilms. Evidence from electron microscopy and fluorescence microscopy reveal the unanticipated internal structure of kidney stones from human patients, where bacterial biofilms are intercalated between polycrystalline mineral layers, even in stones identified as "noninfectious" clinically, including those in patients without underlying urinary tract infections. We observe similar bacterial biofilm architectures on the surfaces of stone fragments obtained due to lithotripsy, suggesting that bacteria are intrinsic to the process of nephrolithiasis. Crystallites proximal to biofilm layers exhibit significantly smaller grain sizes, which indicate a larger local concentration of nucleation sites. Staining reveals that biofilm areas of these stones are enriched with bacterial DNA. That bacteria are now observed so broadly in kidney stones (including even in less prevalent struvite stones) may be conceptually salient: Based on the evidence adduced here, we propose a model in which the urine-rich environment of the kidney can impinge on bacterial calcium homeostasis and amplify bacterial production of nucleation templates such as extracellular DNA. The resultant counterion condensation intrinsic to polyelectrolytes charged beyond the Manning criterion (such as DNA) drastically enhances the probability of heterogeneous nucleation, thereby amplifying calcium oxalate stone formation.

kidney stones | biomineralization | bacteria biofilms

Significance

Bacteria are traditionally believed to contribute only to struvite kidney stone formation. In contrast, most types of kidney stones are believed to be abiotic and considered to be "noninfectious." Here we show that calcium oxalate stones, the most common type of kidney stones, have bacterial biofilms as part of their intrinsic internal structure. In fact, some of the bacteria harvested from such "noninfectious" stones are culturable. These observations may explain the recurrence of kidney stones in some patients, as well as infections caused by stone fragmentation. That bacteria may be endemic to nephrolithiasis suggests the existence of a general conceptual basis for stone formation, which we propose here.

Kidney stone disease prevalence is on the rise globally in recent decades, with a lifetime incidence rate of 1 in 11 people (1–3). Risk factors such as family history, metabolic syndrome, and low fluid intake have been strongly associated with increased incidence of kidney stones (3), and a recurrence rate of up to 80% has been observed in certain compositions (4). Kidney stones are polycrystalline agglomerates, and are categorized based on primary composition. A subset of kidney stones has been previously identified in patients with urinary tract infections (UTIs) (5). Struvite stones ($MgNH_4PO_4.6H_2O$), commonly referred to as "infection stones," are hypothesized to be caused by urease-producing bacteria such as *Proteus* (6), where urease catalyzes the hydrolysis of urea, leading to the promotion of stone production (7). Struvite stones have been reported to have a low incidence rate, roughly 2 to 6% (8, 9), with the vast majority of stones instead being primarily composed of calcium, especially calcium oxalate (CaOx). Calcium-based stones account for over 70% of stones, making them by far the most prevalent type globally (3, 8, 10). These stones are conventionally considered "noninfectious" (i.e., not associated with bacteria) and are polycrystalline agglomerates of crystallites that nucleate based on the Ca and oxalate concentrations present in urine. However, there is emerging evidence that patients with CaOx stones can harbor bacteria on kidney stone culture (11).

The initial formation of CaOx kidney stones is thought to begin with the nucleation and growth of crystallites from supersaturated urine, which aggregate to become sufficiently large to be retained within the urinary fluid flow (12–15). A number of different factors have been investigated in order to target and inhibit CaOx nucleation, growth, and aggregation as a means of preventing stone formation (16–19). Supplements such as potassium citrate and magnesium have been shown to reduce the rate of stone recurrence, likely through a combination of direct inhibition of crystal growth and the reduction of supersaturation of Ca and Ox in urine (13, 17, 20). Hydroxycitrate in particular was shown to have an even stronger inhibitory effect on crystallization, even promoting dissolution in some conditions (21).

Author contributions: W.C.S., A.M., J.L., H.L.S., R.E.S.H., C.L.P.O., S.J.H., A.C., G.C.L.W., and K.B.S. designed research; W.C.S., A.M., J.L., R.Y., G.G.M., H.L.S., R.E.S.H., C.L.P.O., and A.C. performed research; K.B., A.K., D.W., K.D., Q.C., A.C., and K.B.S. contributed new reagents/analytic tools; W.C.S., J.L., H.L.S., and A.C. analyzed data; and W.C.S., A.M., J.L., H.L.S., A.C., G.C.L.W., and K.B.S. wrote the paper.

The authors declare no competing interest.

This article is a PNAS Direct Submission.

[1] W.C.S. and A.M. contributed equally to this work.

[2] To whom correspondence may be addressed. Email: gclwong@seas.ucla.edu or KScotland@mednet.ucla.edu.

This article contains supporting information online at https://www.pnas.org/lookup/suppl/doi:10.1073/pnas.2517066123/-/DCSupplemental.

Phosphates such as pyrophosphate (22, 23), bisphosphonates (24), and hexametaphosphate (20), have also been studied for their inhibitory effects on crystal growth through chelating calcium. Many urinary proteins have also been shown to inhibit CaOx crystal formation and stone growth, such as nephrocalcin (25–28), albumin (27), uromodulin (19, 29), osteopontin (30, 31), and calgranulin (32). Some of these proteins can serve dual purposes, with osteopontin (33), albumin (34, 35), uromodulin (19, 36, 37), either inhibiting or promoting crystallization, depending upon their concentrations, aggregation in solution, or their polymer length. Many synthetic inhibitors have also been designed, utilizing principles derived from the naturally occurring factors listed. Synthetic osteopontin-derived peptides (31), phosphates (38, 39), and polyanionic macromolecules, such as poly(acrylic acid), poly(aspartic acid), and poly(glutamic acid) (19, 40), have all demonstrated efficacy at inhibiting crystallization. Crystal nucleation and growth is a complex process, with many factors capable of functioning as both promoters or inhibitors depending on the exact environmental situation and physical characteristics of the molecule. Thus, a broader understanding of the mechanisms of stone formation will require elucidation of the initial stages of stone nucleation and how different factors can positively or negatively contribute.

Here, we present evidence that suggests an unanticipated parallel mode of kidney stone formation related to the existence of microbial organization. Data from electron microscopy and fluorescence microscopy reveal that layers of bacterial biofilm communities are integrated into polycrystalline mineral layers in CaOx stones, the most prevalent type of kidney stones from human patients, including those from patients without underlying urinary tract infections (UTIs). These observations suggest that homogeneous nucleation of such stones is not the only pathway of formation. Similar bacterial biofilm architectures on the surfaces of stone fragments are observed, suggesting that biomineralization occurs throughout each stone and not just at the surface. Bacterial biofilm communities, known for persistent survival at low metabolic states, are protected by a matrix of secreted exopolysaccharides and extracellular DNA (eDNA). These matrix components, together with other bacterial components such as S-layers, can in principle be efficient nucleation centers and templates for biomineralization of inorganic crystals (41–46). Consistent with this expected increase in heterogeneous nucleation near bacteria, we find that CaOx domain sizes close to bacterial layers are significantly smaller. We propose a model in which a urine-based growth medium can impinge on bacterial Ca homeostasis and amplify production of eDNA nucleation templates for calcium oxalate growth. Taken together, the evidence here suggests that the presence of bacteria can enhance heterogeneous nucleation and thereby stone formation. The identification of this biogenic pathway of stone formation can inform future prevention and treatment of urinary stone disease and stone-induced infections.

Results

Observation of Bacterial Cellular Structure and Biofilm Morphology Observed on Surfaces of Kidney Stones but Not in Abiotic Calcium Oxalate Monohydrate (COM) Crystals. CaOx stones have conventionally been thought to be largely abiotic. However, the vast majority (estimated ~99%) of bacteria in the biosphere are not culturable using standard techniques, due to complex growth requirements, mutualistic interactions with other species in microbiomes, stressed or viable but nonculturable (VBNC) metabolic states (47). Therefore, we sought to further expand our inquiry by utilizing a broad combination of complementary materials science methods sensitive to both physical structure and chemistry. To investigate an association between bacteria and Ca-based kidney stones, we first examine the internal structure of these stones. We used Scanning Electron Microscopy (SEM) to examine various surfaces of patient-derived kidney stone fragments (Fig. 1). Stone fragments analyzed ranged in size from ~0.3 mm to 3 mm in

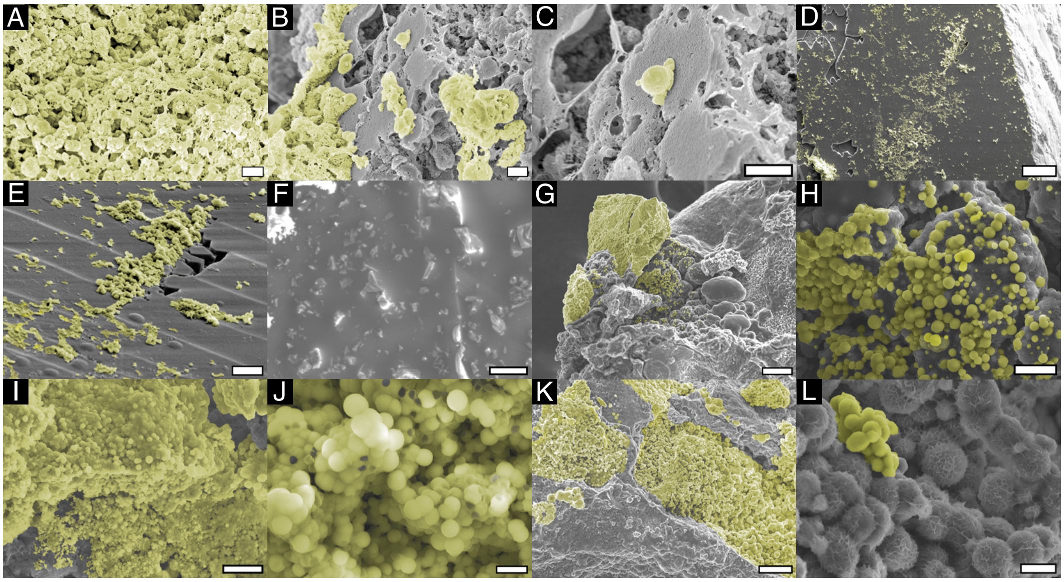

Fig. 1. Scanning electron microscopy of kidney stone fragments. (*A*) Conventional SEM image of a COM kidney stone fragment exhibiting biofilm growth despite testing culture negative (Scale bar, 2 μm). (*B* and *C*) Representative conventional SEM images of a struvite/calcium phosphate (CaP) kidney stone fragment culture positive for *Proteus*. Cells are approximately 0.75 μm in diameter, consistent with most bacteria. (*C*) is a zoomed in image of a region in (*B*) (Scale bar, 1 μm). (*D* and *E*) Conventional SEM images of the surface of a calcium oxalate dihydrate (COD)/CaP/COM culture negative kidney stone fragment with regions of biofilm inhabiting the crystal cleavage planes. (*E*) is a zoomed in image of a region in (*D*) (Scale bar, 10 and 2 μm respectively). (*F*) Representative SEM image of pure whewellite (COM) mineral with no observable bacterial or biofilm structures. (Scale bar, 20 μm). (*G*–*L*) Ionic-liquid coated SEM images of (*G* and *H*) a COM/COD stone fragment which is culture positive for *S. epidermidis*, (Scale bar, 50 and 10 μm respectively) (*I* and *J*) a struvite kidney stone fragment culture positive for *Enterococcus* and exhibiting extensive bacterial colonization, (Scale bar, 10 and 2 μm respectively) (*K* and *L*) a Ca-based (COM/CaP) stone fragment derived from a clinically culture-negative kidney stone, (Scale bar, 50 and 10 μm respectively). (*H*, *J*, and *L*) are zoomed in images of the regions in (*G*, *I*, and *K*), respectively. (*A*–*E* and *G*–*L*) have false coloring (yellow) to indicate regions with bacteria and biofilm present.

diameter (*SI Appendix*, Fig. S1) and stone elemental composition was determined using Raman spectroscopy (*SI Appendix*, Fig. S2), Energy Dispersive X-ray Spectroscopy (EDX) (*SI Appendix*, Fig. S3), and confirmed by the clinical pathology lab using Fourier Transform Infrared Spectroscopy (FTIR). In addition to conventional SEM imaging of sputter coated and ionic liquid coated samples, multiple additional imaging and sample preparation modalities were utilized, including biofilm staining (48), EDX (49), and Focused Ion Beam (FIB) milling (50) in order to obtain a complete picture of the internal organization of stones.

We first compare patient-derived COM stone fragments (Fig. 1*A*) and patient derived struvite fragments (Fig. 1 *B* and *C*). Consistent with what is known regarding the bacterial origin of struvite stones, the distinctive cocci morphology of bacteria was observed. Surprisingly, the same cocci morphology characteristic of bacteria and the fibrous biofilm matrix enveloping bacteria were observed in the presumed abiotic COM stones. These cells were adhered to the surface of the stone fragments, as well as concentrated within the more protected crevices along crystal planes of the stone surface (Fig. 1 *D* and *E*). In contrast, a control sample of pure whewellite (a naturally occurring COM mineral) of abiotic origin was examined using the same methods (Fig. 1*F*) and features consistent with typical whewellite were observed. The control whewellite sample exhibited a smooth, regular surface with sharp angles and smaller crystals scattered on the crystal face, with no structures identifiable as being bacterial in origin.

To preserve the hydrated topography of bacterial cellular structure and biofilm organization, we examine a Ca-based stone fragment that is culture positive for *Staphylococcus epidermidis* under ionic liquid imaging conditions. In these studies (Fig. 1 *G* and *H*), both the typical cellular structure of *S. epidermidis* and its biofilm morphologies were observed in the *S. epidermidis* culture positive sample. As a comparison, we use the same methods on the struvite-based fragments (Fig. 1 *I* and *J*), which are known to be of bacterial origin (51, 52). In a patient-derived struvite stone fragment that is culture positive for *Enterococci*, we also see typical features consistent with cocci morphologies, similar to those previously described by others (48), and commonly found in struvite stones (53). We observed these cocci structures on the surface of both sputter coated and ionic liquid coated samples (Fig. 1 *B*–*L*) with a characteristic size of ~1 µm, consistent with previous measurements (54, 55). Surprisingly, bacteria and biofilm structures were additionally observed within stone fragments which were found to be culture negative for bacteria in clinical testing (Fig. 1 *B*, *K*, and *L*). The unambiguous detection of these bacterial structures in both clinically culture positive and culture negative Ca-based stones indicates that, despite negative culture testing, this type of stone can still contain bacteria and bacterial biofilms, consistent with bacteria being in VBNC metabolic states or in complex mutualistic relationships.

When polished to a flat surface clear striations are present within the internal structure of the stone on Raman spectroscopy (Fig. 2 *A*–*D*). Two distinct types of layers are present, identified by color, with darker bands exhibiting high concentrations of organic material, while lighter bands are composed primarily of calcium oxalate (*SI Appendix*, Fig. S2). Analysis of the crystal domains present in these layers reveals a stark difference in grain size between the organic and crystalline layers (Fig. 2 *D* and *E*). While the organic layers exhibit a relatively uniform characteristic crystal domain size of ~7 µm in diameter, the crystalline layers have a wide range of crystal sizes, with a significantly larger average crystal size of ~236 µm in diameter (Fig. 2*E*). This clear size differential between organic and crystalline layers is representative of the environmental conditions present during each layer's growth. The crystals in the organic layer are limited in their growth and size distribution as a result of a greater concentration of nucleation sites, while those within the crystalline layer have a wide range of crystal sizes, as they are capable of growth in whatever available space is provided to them. There is little size overlap between the two crystal types, with the grains in the crystalline layers having a wide distribution, with only the smallest crystal particles being similar in size to the larger organic crystals.

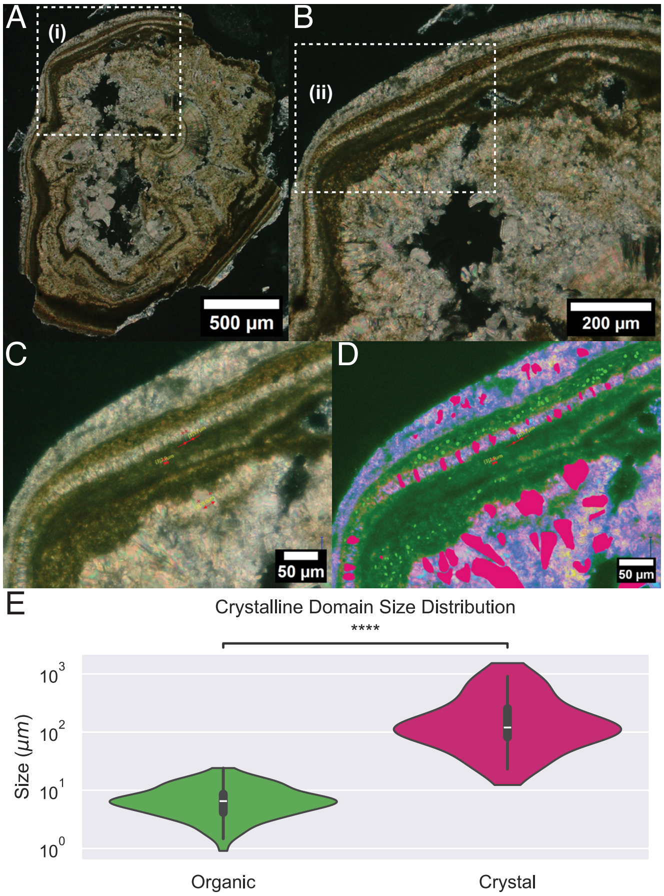

Fig. 2. Crystal domain size distribution (*A*) Light microscopy images of a polished kidney stone fragment. (*B*) Light microscopy image of region (*i*) in panel (*A*). (*C*) Light microscopy image of region (*ii*) in panel (*B*), used for crystal domain comparison. (*D*) Color enhanced image from panel (*C*) with segmented organic (green) and inorganic (pink) crystal domains. (*E*) Size distribution comparison of crystal domains between the organic (green) and crystalline (pink) domains plotted on a logarithmic scale. n = 83 for organic and n = 47 for crystal. Welch's *t* test was used for the statistical comparison (*P*-value: 3.692e-6).

Existence of Bacterial Components within Biofilm Morphologies Observed within Stone Fragments but Not in Abiotic Control Stones. Given the above SEM observations of bacterial cellular structure and biofilm organization within both Ca-based and struvite stone fragments, but not in control mineral samples, we used bacteria and biofilm-specific chemical stains that result in a preferential increase in electron density to demonstrate the chemical existence of bacterial nucleic acids, polysaccharides, and lipid components within these observed morphologies (*Materials and Methods*). In this manner, these bacterial components can be detected directly via increased contrast in SEM imaging (56).

In the control abiotic whewellite mineral fragments, we observed no increase in intensity or contrast compared to the unstained SEM imaging, consistent with the absence of bacteria and biofilm within the sample (Fig. 3 *A* and *B*). In the struvite stone fragments of bacterial origin, the biofilm and bacterial structures were preferentially stained, indicating the presence of lipids, polysaccharides,

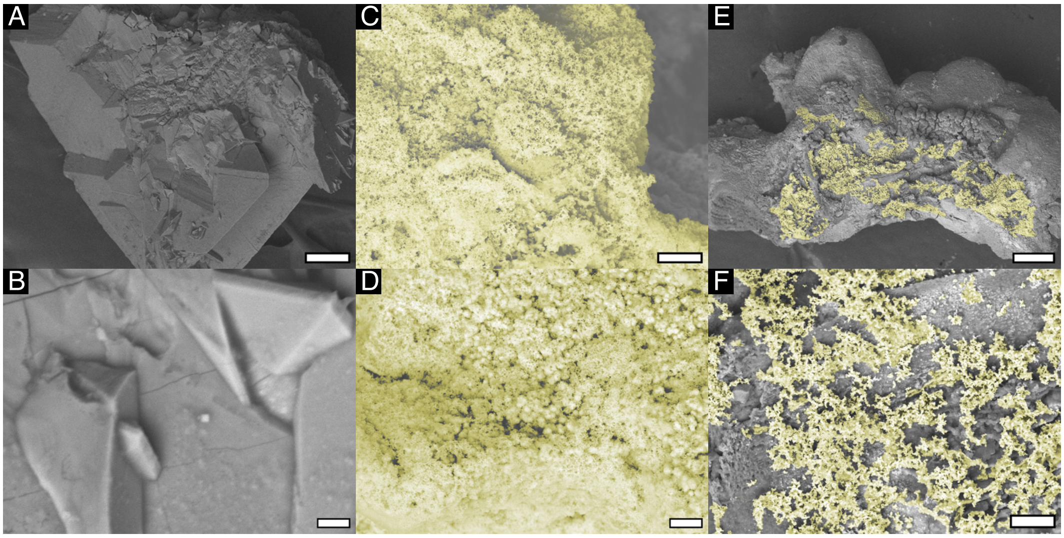

Fig. 3. Biofilm components identified within kidney stones. Ionic-liquid coated SEM images of (*A* and *B*) abiotic whewellite mineral. (Scale bar, 100 and 5 μm respectively). (*C* and *D*) a struvite stone fragment culture positive for *Enterococcus* (Scale bar, 20 and 10 μm respectively) and (*E* and *F*) a clinically culture-negative COM/COD stone fragment exhibiting bacterial biofilm. (Scale bar, 200 and 20 μm respectively). All samples were stained with Osmium tetroxide, Ruthenium Red and UranyLess to stain for lipids, polysaccharides and DNA, respectively. Increased SEM intensity within the biofilm structures indicates preferential stain binding and thus the presence of biofilm components within the structures (false-colored yellow). (*B*, *D*, and *F*) are zoomed in images of the regions in (*A*, *C*, and *E*), respectively.

and/or DNA components (Fig. 3 *C* and *D*). In the standard, culture-negative Ca-based fragments, we see unambiguous evidence of preferential staining of the structures identified by morphology previously as bacterial biofilms, in a manner consistent with the positive control struvite fragments. These observations indicate that the chemical composition of these bacteria-like morphological features is consistent with those found in bacterial biofilms, irrespective of their negative clinical culture tests (Fig. 1*F*).

Dissection of Kidney Stones Using FIB-SEM Imaging Reveals an Unanticipated Lamellar Organic–Inorganic Biocomposite Structure. The data above show how bacterial biofilms can exist on surfaces of Ca-rich kidney stone fragments, which can potentially lead to additional subsequent biomineralization of CaOx on these fragments. To elucidate the internal structure of unperturbed kidney stones, we perform an ex vivo dissection using FIB-SEM, which can sequentially section patient stone fragments in order to reveal their internal structures. Sectioning of the biofilm structures observed on the surface of the clinically culture-negative stone fragments previously described revealed individual cell morphologies embedded within a web-like matrix of dehydrated biofilm (Fig. 4*A* and Movie S1). This biofilm matrix is known to envelop and protect the bacterial colony (57). Consistent with these results, we find that even following dehydration and preparation treatments, the matrix still binds the cells together and adheres them to the surface of the crystalline stone fragment.

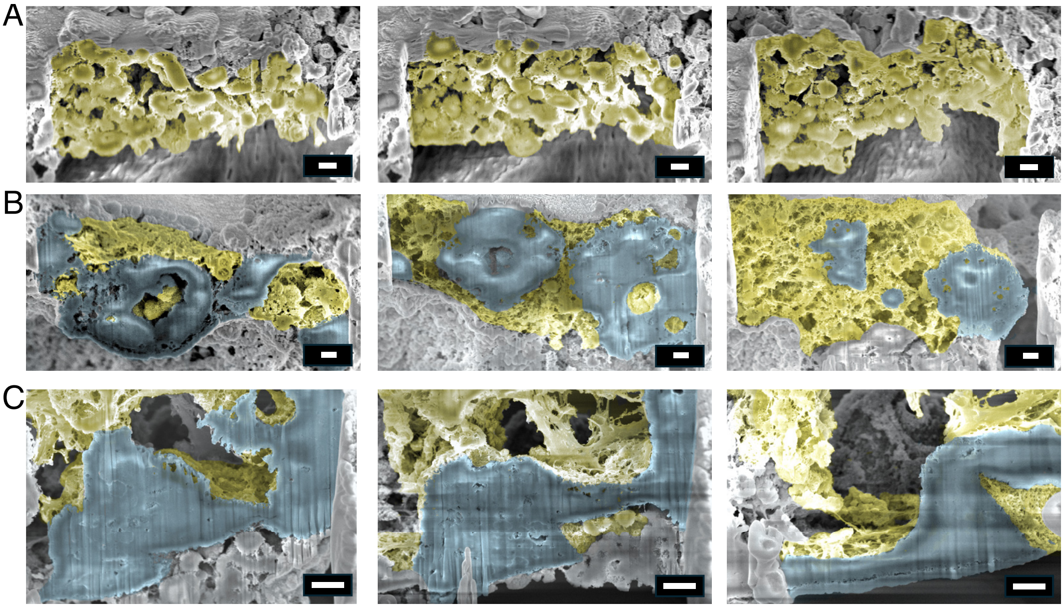

Fig. 4. Bacteria and biofilm identified in voids within kidney stone structures. (*A*) FIB SEM sectioning of the biofilm structures present in a clinically culture-negative COM stone fragment. Distinct *Bacillus* cells and fibrous biofilm matrix are present throughout the sectioning. (*B* and *C*) FIB-SEM sectioning of a struvite stone fragment culture positive for *Proteus*. The voids present within the stone fragment have bacteria and biofilm embedded within them, indicative of the presence of bacteria within the interior of the fragments during stone formation. Full FIB sectioning montages for (*A*–*C*) are presented in Movies S1–S3, respectively. Images are false colored to indicate regions of solid crystal (blue) and biofilm (yellow), respectively. (Scale bar, 1 μm).

When sectioning a stone fragment, large voids were found to be present within the crystal. These voids ranged in size from a few micrometers up to tens of micrometers. We additionally observe morphologies similar to those previously observed on the surface of the fragments, indicative of bacterial biofilm (Fig. 4 *B* and *C* and Movies S2 and S3). These results suggest that bacteria are an integral structural component within kidney stones. We observe these phenomena in every CaOx stone fragment evaluated.

Confocal Imaging Reveals Organization of Polysaccharides and DNA in Biofilm Matrix within Ca-Rich Kidney Stones. In conjunction with SEM imaging, we also utilized fluorescence microscopy in order to determine the organization of matrix components of bacterial biofilms within stones. *Hippeastrum hybrid* lectin (HHL) conjugated to a FITC fluorophore was used to stain for the presence of mannose saccharide motifs, one of the common extracellular polysaccharide (EPS) components of biofilm matrices (58–60). In order to establish a baseline for autofluorescence, fragments derived from the same sample of a CaOx stone identified to be culture positive for *Enterococcus*, were imaged using widefield fluorescence microscopy prior to staining, and minimal autofluorescence in the green channel was observed (Fig. 5*A*). Following staining, the surface of the fragment was found to be preferentially stained in some regions (Fig. 5*B*). While there are a number of urinary glycoproteins which should also be stained by mannose-sensitive lectins, as seen in concanavalin A (61–63), confocal imaging at higher magnification revealed that the lectin preferentially stained cocci structures on the surface of the fragment roughly cell size in diameter (~0.75 μm) and equivalent in morphology to cells previously observed in SEM, indicative of preferential staining of the EPS matrix encasing the bacteria (Fig. 5*C* and Movie S4). In contrast to the kidney stone fragments, the abiotic whewellite mineral control fragment did not show any preferential staining, with low fluorescence signal in all channels both before and after staining and minimal, nonspecific, signal increase in the green channel in response to staining with HHL-FITC (*SI Appendix*, Fig. S4).

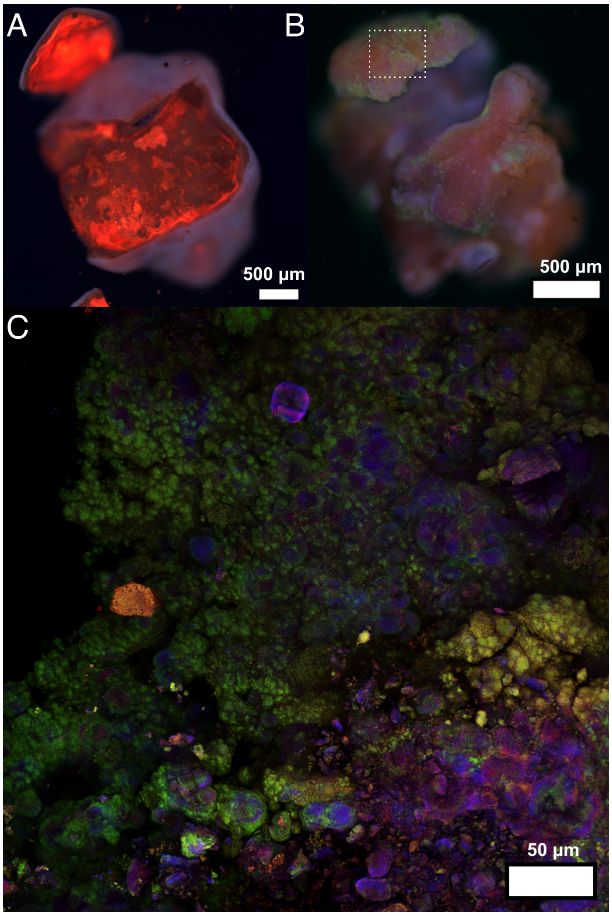

Fig. 5. Fluorescence staining of bacterial biofilm components. (*A* and *B*) Widefield fluorescence microscopy image of calcium oxalate stone fragments culture positive for *Enterococcus* (*A*) unstained and (*B*) stained with HHL-FITC lectin stain for biofilm. (Scale bar, 500 μm). (*C*) Maximal projection image of fluorescence confocal laser scanning microscopy *z*-stack images taken in the region indicated in (*B*, white square). (Scale bar, 50 μm) Confocal fluorescence images of an HHL-stained control whewellite sample are presented in *SI Appendix*, Fig. S4. The full *z*-stack video is presented in Movie S4.

To detect DNA organization with the biofilm matrix, we stained the polished stone fragments with BactoView Live Green DNA cell stain. Minimal autofluorescence in the green channel was observed in the polished samples when imaged in widefield and confocal fluorescence prior to staining (Fig. 6*A*). Following staining with BactoView, we found that the polished stone fragments have large areas of preferential staining, indicative of regions of the stone enriched with biofilm DNA (Fig. 6*B*). Interestingly, these DNA regions cover the surface of the fragment or appear in distinct layers, depending on their orientation relative to the imaging plane of the polished fragment (Fig. 6 *B*–*D* and *SI Appendix*, Fig. S5*A*). Confocal fluorescence microscopy reveals well-defined striations within the fragments which harbor the highest concentrations of bacteria, with high regularity in thickness and periodicity (Fig. 6*C* and *SI Appendix*, Fig. S5 *A* and *B*). At higher magnifications, individual stained bacteria can be resolved on the surface of the polished fragment, with single cells and aggregates being easily identifiable within the stained layers (*SI Appendix*, Fig. S5 *B*–*D*). In contrast, the abiotic whewellite

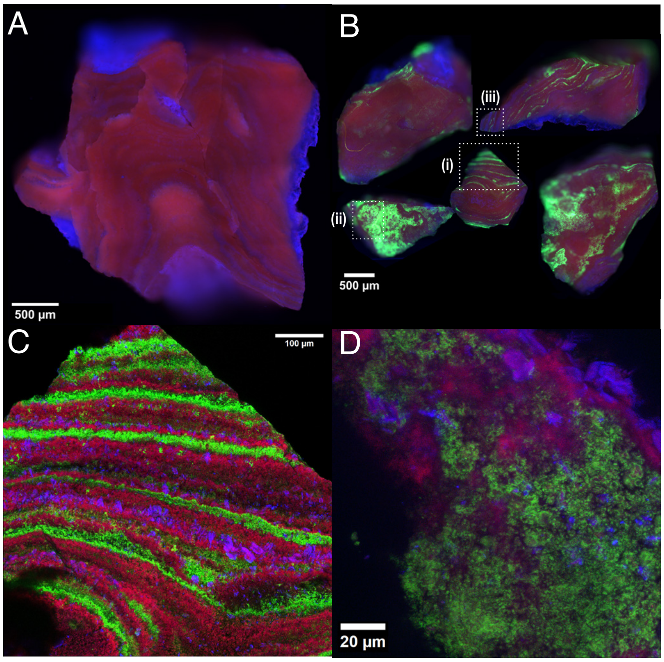

Fig. 6. Bacterial DNA identified within kidney stone layers. (*A* and *B*) Widefield fluorescence images of a COM/COD/CaP kidney stone fragment culture positive for *Staphylococcus* (*A*) before and (*B*) after staining with BactoView Live Green DNA cell stain. Green fluorescence in the sample indicates the presence of bacteria. (Scale bar, 500 μm). (*C*) Fluorescence confocal image of region (a) in panel (*B*). Post acquisition image processing consisted of mosaic merge, Lightning Adaptive Processing, and maximum intensity projection. (Scale bar, 100 μm). (*D*) Maximum intensity projection of a fluorescence confocal image *z*-stack of region (b) in panel (*B*). (Scale bar, 20 μm). Confocal fluorescence images of a BactoView-stained control whewellite sample are presented in *SI Appendix*, Fig. S6.

fragments exhibit no preferential staining with BactoView, indicating the absence of DNA from cells or biofilm matrix (*SI Appendix*, Fig. S6 *A* and *B*). The results of these two fluorescent stains indicate that the biofilm-like structures identified in the SEM imaging are enriched in mannose motifs and also DNA, which are both key components found within the matrix of many bacterial biofilms.

The standard technique for assessing the presence of bacteria in kidney stones involves homogenization of the stone fragments and culture on selective media to measure the number of viable, culturable microbes. Clinical stone cultures obtained in sterile fashion from ureteroscopy or percutaneous nephrolithotomy procedures performed in patients with negative preoperative urine cultures revealed the presence of bacteria in 24 out of 54 stones (*SI Appendix*, Table S1). Given the above-mentioned difficulties with routine culturing of stones, we subsequently used a targeted culturomics strategy using BHI media to isolate and enrich for microbes known to inhabit the urinary tract, including *Escherichia coli, Proteus mirabilis,* and *Enterococcus faecalis*, which were identified using 16S and ITS sequence analysis to capture bacterial and fungal species, respectively (*Materials and Methods*). Patient samples included struvite, uric acid, COM, and mixed CaOx stones obtained after percutaneous nephrolithotomy or ureteroscopy. (*SI Appendix*, Table S2) While many of the stones are composed of struvite or apatite, even those which are wholly or partially CaOx-based still exhibited viable bacteria. 17 of the 22 stones analyzed exhibited culturable bacteria, with cellular concentrations ranging over 6 orders of magnitude (Fig. 7*A*). Sequencing revealed a high degree of diversity in stone microbiomes, with species such as *E. faecalis*, *P. mirabilis*, and *E. coli* among the most common bacterial species identified in these patient samples (Fig. 7*B* and *SI Appendix*, Table S2). Over 30% of assayed stones exhibited some degree of polymicrobial colonization, highlighting the variability and ecological complexity that are capable within the kidney stone environment (Fig. 7*C*). These interdependencies can be difficult to capture in a clinical setting, as the complex and delicate interbacterial relationships can be hard to replicate outside of their natural environments.

Discussion

In this study, we demonstrate the existence of bacteria, bacterial biofilm organization, and biofilm-specific molecular components in calcium-based human kidney stones, which are expected to be abiotic and thereby noninfectious according to convention. Since much of the bacteria in the environment are expected to be nonculturable, we show their presence not simply by culturing but also by using a range of complementary state-of-the-art analysis techniques from materials science. Using these techniques, we find structural and chemical evidence that bacteria are present in struvite stones, where they are expected, and in noninfectious CaOx stones, where they are not. Moreover, we see such evidence of bacteria for calcium oxalate kidney stones that are culture-positive as well as culture-negative, but not in abiotic CaOx crystals, which highlights the sensitivity of our methods. We additionally find a rigid organization between organic and inorganic layers within the stones themselves, with individual bacteria and biofilm being found in the

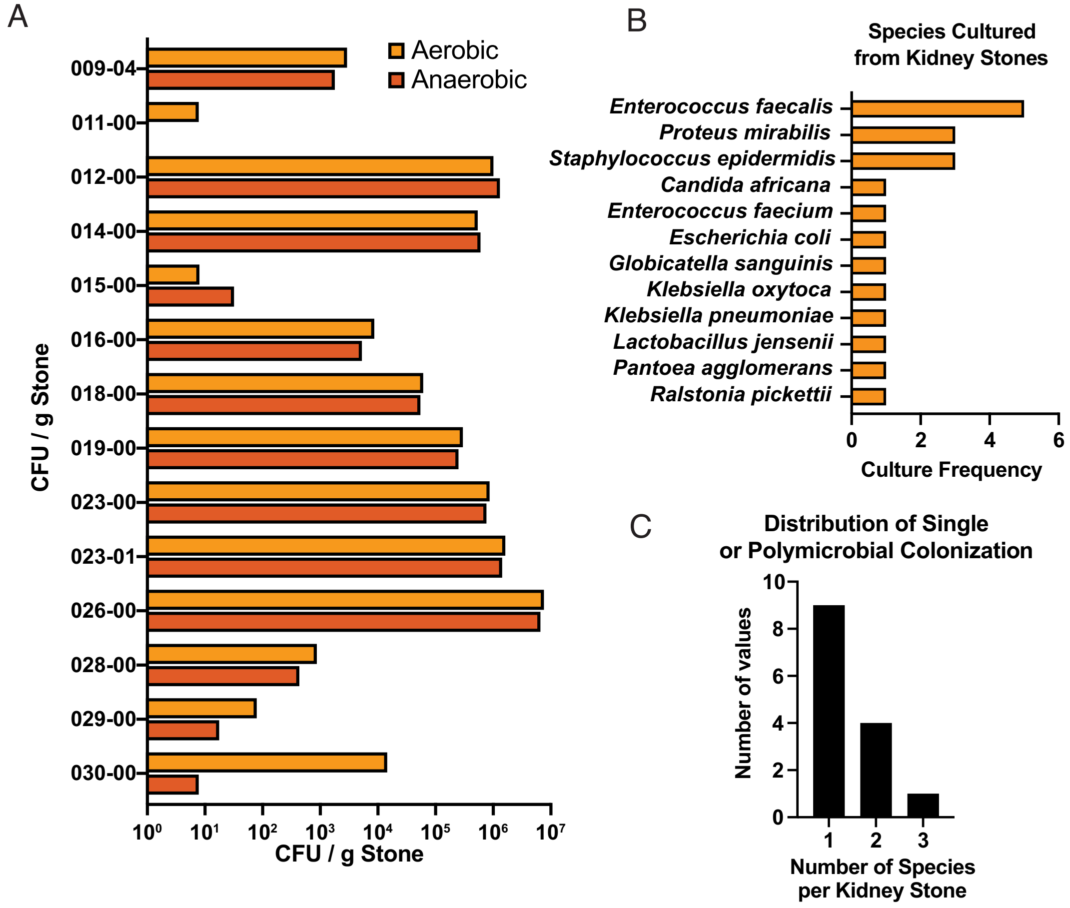

Fig. 7. Kidney stones harbor multiple bacteria. (*A*) Mass-normalized microbial concentrations cultured from various patient samples grown in aerobic and anaerobic conditions. (*B*) Microbial species identified in the cultures from (*A*). (*C*) Distribution of the number of species identified in individual stone fragment cultures in (*A*).

former. Taken together, these observations suggest a model that the architecture of the kidney stones consists of an organic–inorganic biocomposite, where the bacterial biofilms are an integral part of the stone, even in cases where conventional clinical culture testing would suggest the lack of bacterial presence.

The methods we use have been adapted specifically for this study on biofilms associated with kidney stones. Conventional sputter coated SEM is not optimal for these studies: While the rigidity of bacterial cell walls allows them to more easily retain their structure during preparation, the naturally hydrated biofilm experiences significant volume loss and deformation during the dehydration steps (64). As a result, biofilm imaging in SEM often results in well-defined bacteria, but the hydrated biofilm matrix is reduced to a collection of stringy features connecting the cells it previously encapsulated (Fig. 1 *B–D*). To better preserve the morphology of the biofilm itself, and to minimize disturbance induced by dehydration during sample preparation, we used ionic liquid drop casting to maintain the natural hydration state of the biofilm (Figs. 1 *G–L* and 2) (65, 66). The samples embedded in ionic liquid retained the well-known elements of biofilm structure, with both the matrix and embedded cells clearly visible on the surface of the stone fragments. Both the gold sputter coated and ionic liquid coated stone fragment images stand in stark contrast to those of the abiotic whewellite fragments. While the crystalline structures observed on the face of the whewellite fragments were similar to those found in the kidney stone fragments, the lack of any morphology characteristic of biofilm was indicative of their abacterial origin.

Interesting to note is that samples confirmed to be mineralogically CaOx by Raman spectroscopy still exhibit a strong phosphorus signal in EDX mapping (*SI Appendix*, Fig. S3). Despite extensive Raman spectroscopic examination confirming pure COM mineralogy, no detectable phosphate signatures—including the diagnostic v_1 symmetric stretching mode at ~960 cm^{-1} and v_3 antisymmetric stretching modes at ~1,075 cm^{-1}—were observed. One possible explanation for this difference is that Raman requires sufficient crystalline order to generate detectable vibrational signatures above background level noise, suggesting that the phosphorus observed in EDX is either noncrystalline in origin or that the phases present exist in forms incompatible with dispersive Raman detection. Overall, the lack of detectable P-O vibrational modes in Raman analysis indicates that the patient samples analyzed are primarily composed of CaOx mineralogically.

We adduce a range of evidence to demonstrate the chemical existence of bacteria and bacterial biofilms in these stone fragments. First, we employ specific electron microscopy stains typically used for positive identification of bacterial biofilm features (48). Sequential staining of stone samples with osmium tetroxide, ruthenium red (67), and a uranyl acetate substitute (Uranyless), are used to highlight lipids, EPS, and DNA, which are common components of biofilms (56). We find that the bacterial biofilm morphological features identified from SEM colocalize reliably with regions that are strongly stained by these factors. Second, we use confocal imaging to identify chemical features that are common in bacterial biofilms. These include mannose residues in bacteria exopolysaccharides (HHL-FITC stain), and DNA within cells as well as eDNA within the matrix structure (BactoView DNA cell stain). Both single cells and clusters within biofilm aggregates were easily identifiable by their cell-shaped morphologies, being present both on the surface of the fragments as well as within their own distinct layers in the polished stones. In contrast to the distinctive biofilm features observed in the patient fragments, when abiotic whewellite fragments were stained with HHL or BactoView there was no preferential staining and no identifiable presence of bacteria. The presence of these distinct, well-defined striations suggests that mineralization and biofilm growth may be cyclic in time and/or individual crystallites with biofilms aggregate with time.

Bacteria are detected on the surfaces of calcium oxalate kidney stone fragments. Interestingly, bacteria are also detected within the interior of kidney stones, as evidenced by FIB-SEM in situ sectioning under ultrahigh vacuum (UHV, 10^{-10} torr) conditions. We found that within the conventionally prepared and sputter coated stone fragments, there were voids with bacteria and biofilm present. This result, along with the confocal microscopy images of bacterial layers suggest that biofilm is present throughout stone growth. We hypothesize that they provide nucleation sites for mineralization at all stages of growth, rather than just colonizing the surface of the mature stones at the end of development, as previously thought (46, 68). These voids had been previously shown to be formed following dissolution and recrystallization during the formation of kidney stones, as well as from the aggregation of smaller crystallites to form larger, polycrystalline kidney stones (69–71). The intrinsic voids in such polycrystalline kidney stones may allow bacteria limited nutritional access and thereby persistence within stones, which is especially important given that Ca is not an energetically favorable electron acceptor for bacterial extracellular electron transfer (EET), compared to Fe or Mn for example (72).

Some studies have investigated the role that bacterial biofilm may play in struvite stone formation in vitro and have found that the presence of bacteria leads to increased stone growth (73, 74). It has been hypothesized that ureolytic bacteria on struvite can generate areas of increased pH, leading to increased mineral precipitation, but the mechanisms are not fully understood (75). What happens in general in nephrolithiasis, especially for the Ca-rich stones is unknown.

The results here show that CaOx stone formation is associated with the existence of bacterial biofilms and biofilm components. While it can be argued that such components can lead to enhanced heterogeneous nucleation of inorganic crystals, what remains unknown is why there is association between bacterial biofilms and Ca-rich stones in the urine rich kidney environment to begin with. From the perspective of microbial metabolism and homeostasis: Bacteria have to maintain a large Ca gradient in order to remain viable (~100 nM intracellular and ~1 mM extracellular Ca concentration) (76), which is accomplished using ATPases to pump Ca out of the cell (77). This metabolic burden is exacerbated by the biofilm mode of existence and the general unsuitability of Ca for EET. Biofilms are known to produce eDNA, either through secretion or release through lysis of a subpopulation of cells. Such externalized DNA provides an effective extracellular "Ca sponge": As a rough estimate, lysis of a single bacterium contributes ~4 Mb of DNA, which will locally sequester ~3.6×10^6 divalent Ca ions, based on a rough numerical estimate from Manning condensation (78). The fraction of charge neutralized by multivalent counterions is $f = 1 - 1/(Z\xi)$. Here, Z = valence of the multivalent ion; ξ = Manning parameter = λ/b; λ = Bjerrum length of water, roughly 7.8 Å; b = distance between charges on DNA, or equivalently the inverse of the linear charge density of DNA. For divalent Ca ions, $f = 0.89$. Numerical estimates based on the nonlinear Poisson–Boltzmann formalism and measurements of divalent ion concentrations condensed near DNA using anomalous X-ray scattering experiments (79–81) are in qualitative agreement with this estimate. The condensation of multivalent ions like Ca and Mg dominate monovalent ions such as Na on polyelectrolytes due to entropy.

Since extracellular Ca ions are not uniformly distributed in space but mostly confined to condensed ion "sheaths" around eDNA, the stringent Ca pumping required for homeostasis can be greatly alleviated. In the case of urine, the requirement for Ca pumping is even more stringent: the extracellular Ca level can now be up to 7 mM Ca (82). Not surprisingly, recent measurements show that *Pseudomonas aeruginosa* cultured in urine secrete anomalously large amounts of eDNA (83). In other words, the urine environment can induce the bacterial release of eDNA "dressed" with Ca ions, which function as an anionic nucleation template for calcium oxalate formation by locally increasing Ca concentrations and spatially organizing such ions at molecular distances. Previously, DNA has not been thoroughly investigated as a factor in driving kidney stone formation and growth as a result of being only a small fraction of the total organic component of the mature stones (19, 84). There is in fact a large corpus of work that shows that the anionic ridges of the sugar-phosphate backbone of DNA can be a molecular template for crystallization of inorganic crystals, and others which show that anionic organic macromolecules may play a role in nucleation and aggregation of CaOx crystals by binding surface Ca (19, 85–88). When compared to these polyanionic macromolecules, we find that as opposed to the weakly charged polymers, DNA exhibits a dense negative charge. Poly(glutamic acid) [poly(E)] and poly(aspartic acid) [poly(D)] have a linear charge density of roughly 1.3 e^- per nm, while DNA has a density of approximately 5.8 e^- per nm, more than fourfold greater. This results in a Manning parameter of ~1.01 compared to ~4.5 of eDNA. The charge density of the poly(amino acid) chains is thus at best marginally enough for idealized Manning condensation even in the absence of monovalent ions. In contrast, the charge density of DNA is well over the Manning limit ($1e^-/l_B$), where l_B is the Bjerrum length in water (~0.71 nm). At physiological monovalent salt levels (~100 mM NaCl), however, there is strong competition from Na condensation. Therefore, even though divalent ions are in principle entropically favored over monovalent ions in counterion condensation, we expect significantly less divalent Ca cation condensation in poly(E) or poly(D) compared to DNA, and hence much less Ca templating for biomineralization. These effects are not limited to just bacterial eDNA, as other groups have reported that neutrophil extracellular traps (NETs), networks of DNA secreted by neutrophils to bind and neutralize pathogens, have also been implicated in the formation of both kidney stones and gallstones (89, 90). Thus while the weakly charged synthetic polymers may inhibit nucleation and aggregation, the stronger, stiffer, and longer DNA can potentially drive stronger Ca condensation and organization which will lead to promotion of crystal nucleation and aggregation. It is also noteworthy that the most prevalent species of bacteria associated with kidney stones are also species known to secrete eDNA, *E. coli*, *P. aeruginosa*, *K. pneumoniae*, *E. faecalis*, *S. epidermidis*, *P. mirabilis* (91–93).

Our data showing the strong association of bacterial biofilms with Ca-rich stones are consistent with this proposed model. The BactoView DNA labeling is expected to preferentially stain DNA within dead cells with compromised membranes and/or externalized DNA. Our data show that the fluorescence from DNA labeling is anomalously strong and spatially extended, which is not inconsistent with eDNA staining. The small calcium oxalate crystalline domain sizes near bacterial layers are also consistent with the existence of higher concentrations of nucleation centers. Clearly there will be other effects that stem from eDNA (94, 95), which are known to influence the strength of the biofilm matrix. Equally apparent is the existence of other templates for nucleation besides eDNA. Osteopontin (33), albumin (34, 35), and uromodulin (19, 36, 37) have all been shown to be capable of promoting CaOx stone formation in certain conditions, rather than their traditional roles as inhibitors, and other factors such as lactoferrin and lysozyme have also been shown to promote stone formation (96). Certain combinations of polycationic and polyanionic macromolecules has also been shown to be capable of aggregation that can drive CaOx nucleation and crystal growth (19). In addition to CaOx, L-cystine has been shown to crystallize into stones, and specialized molecules have been designed to bind and inhibit their growth (97–99). Another recent in vitro study observed how levan, an exopolysaccharide component of some biofilms, induced the formation of COM and dihydrate crystals (46). Kidney stone formation is a complicated process likely involving a number of different factors including supersaturation and urinary proteins, and while whether bacterial biofilm and eDNA are a principal mechanism of stone nucleation and growth remains to be further explored, it is clear that they can serve as a contributing factor in the formation. Here, we attempt to show how the urine environment can amplify the tendency for stone formation by making requirements for bacterial homeostasis more stringent and thereby promote release of nucleation templates for crystallization.

The presence of bacteria within stones is also important to consider with regard to kidney stone related infections. Stone episodes can be complicated by infections that may lead to serious illness (5, 100). Our study demonstrated that the bacterial presence within kidney stones is pervasive across several stone types, and thus it is important to account for the possibility of contribution from otherwise undetected bacteria which may be present within the stone composition and could be contributing to stone related infections directly or by potentiating stone growth through mineral precipitation and exacerbating obstruction. In the case of the former, there are significant debates among microbiologists regarding the limits of cell viability and when a cell should be considered to be dead and not metabolically dormant (101). Indeed, in some instances, while a bacterium may be nonviable in one growth condition, if given sufficient time to resuscitate in another condition, it can be capable of growth and replication. Thus, in this instance, although the bacteria may appear nonviable in clinical lab culture tests, the possibility still remains that when released from within the stones during fragmentation, the environment may be suitable enough that, given sufficient time for resuscitation, the bacteria cells may be capable of growth and infection.

Understanding the exact role biofilm may play in calcium-based stones could have revolutionary implications for treatment and prevention of most common kidney stones. There are currently very few treatment options available for calcium stones. The current therapies for prevention of calcium-based stone growth include dietary changes, hydration, and surgical removal (102). Additionally, while antibiotic treatment has also been considered for prevention of recurrent struvite "infection stones," antibiotics carry the additional high risk of developing antibiotic resistance. Given the role that biofilm may play in the formation and development of this type of stone, therapies aimed at biofilm prevention and elimination could have great potential as anti-stone treatment modalities in the future (103).

Conclusion

In conclusion, we found that irrespective of culture positivity, bacteria and biofilm were present on human calcium-based kidney stones and may play a causative role. We present a model that relates stone formation to the Ca homeostasis requirement in bacteria. These results could have future clinical implications for how we treat and prevent these types of kidney stones and future studies are necessary to understand the interaction between bacteria and calcium kidney stones.

Materials and Methods

Specimen Collection and Storage. Kidney stone fragments were collected under sterile conditions from male and female human patients during ureteroscopy with laser lithotripsy (IRB# 22-001886). Fragments were then further fragmented under sterile conditions and subsequently utilized for all imaging experiments. Half of the fragments from each stone were sent for culture and composition analysis by the Institutional Clinical Pathology laboratory. The remaining fragments were stored in 0.9% saline solution and frozen at −20 °C for analysis.

The sample of whewellite mineral of abiotic origin utilized as a negative control for these experiments was obtained from the Mineral Sciences collection at the Natural History Museum of Los Angeles County (catalog #30417, Saxony, Germany). The specimen was mechanically fragmented in order to obtain samples of approximately 1 to 2 mm in diameter, roughly equivalent in size to the kidney stone fragments, and stored under sterile conditions to prevent potential contamination.

Light Microscopy. Stone fragments were imaged using a VHX 5000 Digital Microscope (Keyence) with a VH-Z20R/W/T objective (Keyence) at 100× magnification.

Raman Spectroscopy. Stone fragments were manually polished into flat thin sections using a 6″ lapidary grinding and polishing machine (Hi-Tech Diamond) prior to spectroscopy. Light microscopy images of thin sections were initially digitized using an optical microscope integrated within the XploRa PLUS micro-Raman spectrometer (HORIBA). Thin sections were stitched as a mosaic using a "Mosaic Area" tile scan function in the LabSpec 6 software platform (HORIBA Scientific) at 100× magnification (0.9 NA). The LabSpec6 "Rectangle" and "Diagonal Line" functions were then used to map out and scan regions of interest (as an area and line scan, respectively) on thin sections with step sizes ranging from 0.4 to 2.7 μm.

Raman spectroscopy was performed on an XploRa PLUS micro-Raman spectrometer (HORIBA) using the following acquisition parameters: incident wave of 532 nm, 200 μm entrance slit, 100 μm confocal pinhole, 1,200 g/mm diffraction grating, 50% filter with laser intensity of 12.25 μW, and a 100× (0.9 NA) objective. Raman spectra were collected from 100 cm^{-1} to 2,500 cm^{-1}. Spectra baseline subtraction and peak fitting were performed using a combination of the "Baseline Correction" function in the LabSpec6 software platform and a Gaussian peak shape (at fit intervals between 1,420 cm^{-1} and 1,535 cm^{-1}) in the MagicPlot program. To distinguish oscillatory patterns of organic and crystalline material in our polished stone fragments, a custom spline fit curve in the MagicPlot program was applied.

SEM.

Sample fixation and mounting. Samples were fixed with 2.5% glutaraldehyde and 4% paraformaldehyde in 100 mM phosphate buffered saline (PBS) (Sigma-Aldrich, BioUltra) overnight at 4 °C. Following fixation, samples were washed three times with 100 mM PBS, then stained with 1% OsO_4 (Sigma-Aldrich, 75632) in 100 mM PBS for 2 h at 4 °C. Samples were then dehydrated in a graded ethanol series of 30%, 50%, 70%, 90%, and 100% for 15 min each before being dried with hexamethyldisilazane (HMDS) (Sigma-Aldrich, reagent grade, ≧99%) in a vacuum desiccator overnight. Each sample was mounted on a standard stub 32 mm pin mount (Ted Pella Inc.) using double-sided carbon tape. Prior to imaging, samples were sputter coated with gold for 30 s to form a thin conductive layer of around 6 to 20 nm on the surface.

Conventional and FIB-SEM imaging. Conventional SEM and cross-sectional FIB-SEM imaging were performed on the sputter coated samples using the Helios 600i dual-beam system (FEI Company). An electron beam with an accelerating voltage of 5 to 10 kV and current of 0.17 nA to 1.4 nA was used for imaging. Prior to FIB sectioning, a protective platinum layer of 200 nm thickness was deposited at 0.23 nA using FIB to avoid charging effects. FIB was performed at 30 kV, and an ion beam current of 9.3 nA was used to cut a large window with a width of about 10 to 20 μm for cross-section viewing, while 2.5 nA was used for cleaning the cross-section.

EDX mapping. EDX mapping for dehydrated samples was performed on the sputter coated samples using a Scios 2 DualBeam system (Thermo Fisher Scientific) equipped with an Octane Elite Super EDS detector (EDAX). An electron beam with an accelerating voltage of 20 kV and current of 0.2 nA was used for mapping.

Ionic liquid drop casting.

Sample fixation and mounting. A modified ionic liquid protocol (65, 66) was used for electron-lucent conductive coating. Ionic liquid (1-butyl-3-methylimidazolium tetrafluoroborate) was diluted to 0.22 M (5 wt.%) in deionized water. Thawed stone specimens were placed in well plates containing 100 μL of ionic liquid. Excess liquid was wicked using a KimWipe (Kimberly Clark) and the samples were mounted on an aluminum stub using double-sided carbon tape.

Conventional imaging. The ionic liquid coated samples were imaged using a JSM-IT200 Scanning Electron Microscope (JEOL USA). The specimens were imaged under high vacuum at 15 kV, 40 mA, with a working distance of 9.8 mm. All images were obtained with a secondary electron detector, and both conventional imaging and energy dispersive spectra were acquired simultaneously. Magnifications ranged from 500× to 20,000×.

Biofilm staining. A modified biofilm staining protocol was used to stain different matrix components for identification (55). Specimens were thawed and then soaked in 0.004 M OsO_4 solution for 30 min for fixation and lipid staining. Samples were then washed with deionized water and placed in 250 mL of 0.001 M Ruthenium Red solution for 30 min to 1 h to stain polysaccharides. The specimens were then placed in UranyLess (Delta Microscopies), a lanthanum-based uranyl acetate substitute, for 2 to 4 min to stain for DNA groups. Last, the specimens were coated with ionic liquid and imaged in the same manner as previously described, with the addition of using a backscattered electron detector (BSED) to better capture contrast differences induced by the stains.

Fluorescent Light Microscopy.

Sample preparation. For flat samples, stone fragments were manually polished to a flat surface prior to staining. The fragments, or a representative fragment derived from the same kidney stone sample, were imaged prior to staining to establish a baseline for sample autofluorescence. Samples were then submerged in 100 μL of 1 μg/mL *Hippeastrum* Hybrid Lectin (HHL) (bioWORLD) conjugated with FITC in ultrafiltered deionized water, or 100 μL of 1× BactoView Live Green (Biotium) in Dulbecco's Phosphate Buffered Saline (DPBS) (Sigma-Aldrich) for 30 min before being washed 3× with ultrafiltered deionized water or DPBS, respectively. Samples were embedded in 1% agarose within a μ-Slide 8 Well coverslip (ibidi) for imaging.

Widefield fluorescence microscopy. Samples were imaged on a DMi8 (Leica Microsystems) inverted microscope using a 5× air (NA = 0.15) or 10× air (NA = 0.3) objective. Samples were imaged in DAPI (20 ms), GFP (30 or 50 ms), and Rhodamine LP (20 or 40 ms) fluorescence channels using a Leica DFC7000T digital color camera (Leica Microsystems), with unstained and stained images of the same sample using identical exposure settings. Image size = 1,920 × 1,440 pixels. Larger samples were imaged using a tile scan and stitched using the Leica LASX "Mosaic Merge" function (Leica Microsystems) when appropriate. *SI Appendix*, Fig. S5*A* was additionally processed with the Leica LASX "Extended Depth of Field" (EDOF) function to combine multiple depths of focus.

Confocal laser scanning microscopy. Samples were then imaged on a Leica TCS-Sp8 confocal microscope (Leica Microsystems) using a 63× oil immersion (NA = 1.4) or 20× oil immersion (NA = 0.75) objective with a scan speed of 700 Hz. Laser and detection information for Blue, Green, and Red fluorescence channels are as follows. For the blue channel, laser excitation wavelength was 405 nm, 10% or 20% laser power, and a Power Hybrid Detector (HyD) (Leica Microsystems) with spectral position of 410 nm to 470 nm was used for detection of autofluorescence emission. For the green channel, laser excitation wavelength was 488 nm, 0.5% or 8% laser power, and a Photomultiplier Tube (PMT) detector (Leica Microsystems) with spectral position of 510 nm to 530 nm was used for detection of emission for both autofluorescence (unstained samples) and the biofilm stains (stained samples). For the red channel, laser excitation wavelength was 552 nm, 3%, 7% or 8% laser power, and a HyD with spectral position of 570 nm to 610 nm was used for detection of autofluorescence emission. Laser power settings were unaltered between images which are directly compared, and images were collected as a "by line" sequential scan to avoid crosstalk between channels. Image size = 1,024 × 1,024 pixels.

Larger confocal images were tile scanned and stitched using the "Mosaic Merge" function as previously described, and *z*-stack images were combined into maximal intensity *z*-projections using the Leica LASX function "Projection" with the maximum method. Fig. 4*C* was additionally processed using the Leica LASX deconvolution function "Lightning Adaptive Processing."

Stone Culturing and Sequencing. This study was conducted with the approval of and under the supervision of the Institutional Review Board of Washington University School of Medicine in St. Louis, MO (IRB# 201410058). Adults over 18 y old who were seen at Barnes Jewish Hospital (St. Louis, MO) who were diagnosed with kidney stones were approached as potential participants and those who were willing and able to sign informed consent forms were enrolled. Participants underwent kidney stone removal surgery, as per standard of care protocols, and the kidney stones were collected intraoperatively. Kidney stones were then transported to the Washington University School of Medicine for processing in less than 2 h. Kidney stones were weighed, washed with PBS, and then pulverized using micropestles in 1 mL of PBS. The stones were vortexed and then sonicated for 10 min to dislodge microbes, serially diluted, and plated onto brain heart infusion (BHI, Becton Dickinson) agar plates. These plates were then grown at 37 °C either aerobically or sealed in anaerobic chambers with GasPak (Becton Dickinson) anaerobic gas sachets. After 24 h of incubation, total microbial burden in the stones was counted on the serial plates and every distinct colony morphotype was collected and struck onto BHI agar plates. These colony morphotypes were sequentially collected and restruck until single morphotypes were present on a plate. These agar plates were sent for 16S sequencing at GeneWiz and matched to microbial species using the NCBI BLAST database. The alignments were manually curated to identify the most likely bacterial species based on query coverage and identity score. In instances where the 16S sequencing failed, ITS sequencing was used instead to identify fungal isolates, following the same query methodology.

Data, Materials, and Software Availability. Data and scripts used to generate the plots in the figures are available at https://figshare.com (DOI: 10.6084/m9.figshare.31014964) (104).

ACKNOWLEDGMENTS. K.B.S. is supported by the NIH (1K08DK132486-01A1 and KL2TR001882-06). W.C.S., R.Y., and G.C.L.W. are supported by NIH R01AI143730 and NSF DMR2325840. W.C.S. is also supported by NSF Graduate Research Fellowship Program (DGE-1650604, DGE-2034835) and by the Ruth L. Kirschstein National Research Service Award "Multidisciplinary Training in Microbial Pathogenesis" (T32AI007323). J.L. and Q.C. are supported by funding from the Air Force Office of Scientific Research under the award number of FA9550-23-1-0609 and the Chan Zuckerberg Biohub Chicago. H.L.S., R.E.S.H., C.L.P.O., K.B., A.K., and S.J.H. are supported by NIH R01DK051406. Confocal laser scanning and widefield microscopy was performed at the Advanced Light Microscopy/Spectroscopy Laboratory and Leica Microsystems Center of Excellence at the California NanoSystems Institute at UCLA (RRID:SCR_022789) with funding support from NIH Shared Instrumentation Grant S10OD025017 and NSF Major Research Instrumentation grant CHE-0722519. We also thank the CNSI Voucher Award program for support in funding this work. SEM was performed at the Materials Research Laboratory at University of Illinois, Urbana-Champaign and at the Natural History Museum of Los Angeles County UNLAB, NSF RaMP-2216721.

Author affiliations: [a]Department of Bioengineering, University of California Los Angeles, Los Angeles, CA 90095; [b]Department of Chemistry and Biochemistry, University of California Los Angeles, Los Angeles, CA 90095; [c]Department of Microbiology, Immunology, and Molecular Genetics, University of California Los Angeles, Los Angeles, CA 90095; [d]California NanoSystems Institute, University of California Los Angeles, Los Angeles, CA 90095; [e]Department of Urology, University of California Los Angeles, Los Angeles, CA 90095; [f]Department of Materials Science and Engineering, University of Illinois Urbana-Champaign, Urbana, IL 61801; [g]Department of Mineral Sciences, Natural History Museum of Los Angeles County, Los Angeles, CA 90007; [h]Department of Molecular Microbiology, Washington University School of Medicine, St. Louis, MO 63110; [i]Center for Women's Infectious Disease Research, Washington University School of Medicine, St. Louis, MO63110; [j]Department of Surgery, Division of Urologic Surgery, Washington University School of Medicine, St. Louis, MO 63110; [k]Department of Chemical and Biomolecular Engineering, University of Illinois Urbana-Champaign, Urbana, IL 61801; [l]Beckman Institute for Advanced Science and Technology, University of Illinois Urbana-Champaign, Urbana, IL 61801; and [m]Chan Zuckerberg Biohub Chicago, Chicago, IL 60642

1. V. Romero, H. Akpinar, D. G. Assimos, Kidney stones: A global picture of prevalence, incidence, and associated risk factors. *Rev. Urol.* **12**, e86–e96 (2010).
2. C. D. Scales, A. C. Smith, J. M. Hanley, C. S. Saigal, Prevalence of kidney stones in the United States. *Eur. Urol.* **62**, 160–165 (2012).
3. K. Stamatelou, D. S. Goldfarb, Epidemiology of kidney stones. *Healthcare* **11**, 424 (2023).
4. M. Daudon, P. Jungers, D. Bazin, J. C. Williams, Recurrence rates of urinary calculi according to stone composition and morphology. *Urolithiasis* **46**, 459–470 (2018).
5. B. Thomas, D. Tolley, Concurrent urinary tract infection and stone disease: Pathogenesis, diagnosis and management. *Nat. Rev. Urol.* **5**, 668–675 (2008).
6. N. Karki, S. W. Leslie, "Struvite and triple phosphate renal calculi" in *StatPearls* (StatPearls Publishing, 2023).
7. H. L. T. Mobley, G. L. Mendz, S. L. Hazell, Eds., *Helicobacter pylori: Physiology and Genetics* (ASM Press, 2001).
8. G. Kravdal, D. Helgø, M. K. Moe, Kidney stone compositions and frequencies in a Norwegian population. *Scand. J. Urol.* **53**, 139–144 (2019).
9. J. S. Rodman, Struvite stones. *Nephron* **81**, 50–59 (1998).
10. P. Singh *et al.*, Stone composition among first-time symptomatic kidney stone formers in the community. *Mayo Clin. Proc.* **90**, 1356–1365 (2015).
11. E. Barr-Beare *et al.*, The interaction between *Enterobacteriaceae* and calcium oxalate deposits. *PLoS One* **10**, e0139575 (2015).
12. B. Finlayson, F. Reid, The expectation of free and fixed particles in urinary stone disease. *Invest. Urol.* **15**, 442–448 (1978).
13. D. J. Kok, S. E. Papapoulos, O. L. Bijvoet, Crystal agglomeration is a major element in calcium oxalate urinary stone formation. *Kidney Int.* **37**, 51–56 (1990).
14. D. J. Kok, S. R. Khan, Calcium oxalate nephrolithiasis, a free or fixed particle disease. *Kidney Int.* **46**, 847–854 (1994).
15. S. R. Khan, Histological aspects of the "fixed-particle" model of stone formation: Animal studies. *Urolithiasis* **45**, 75–87 (2017).
16. K. P. Aggarwal, S. Narula, M. Kakkar, C. Tandon, Nephrolithiasis: Molecular mechanism of renal stone formation and the critical role played by modulators. *Biomed. Res. Int.* **2013**, 292953 (2013).
17. W. G. Robertson, Do "inhibitors of crystallisation" play any role in the prevention of kidney stones? A critique. *Urolithiasis* **45**, 43–56 (2017).
18. D. J. Kok, W. Boellaard, Y. Ridwan, V. A. Levchenko, Timelines of the "free-particle" and "fixed-particle" models of stone-formation: Theoretical and experimental investigations. *Urolithiasis* **45**, 33–41 (2017).
19. J. D. Rimer, A. M. Kolbach-Mandel, M. D. Ward, J. A. Wesson, The role of macromolecules in the formation of kidney stones. *Urolithiasis* **45**, 57–74 (2017).
20. T. Robinson *et al.*, Hexametaphosphate as a potential therapy for the dissolution and prevention of kidney stones. *J. Mater. Chem. B* **8**, 5215–5224 (2020).
21. J. Chung *et al.*, Molecular modifiers reveal a mechanism of pathological crystal growth inhibition. *Nature* **536**, 446–450 (2016).
22. H. Fleisch, S. Bisaz, Isolation from urine of pyrophosphate, a calcification inhibitor. *Am. J. Physiol.* **203**, 671–675 (1962).
23. H. Fleisch, S. Bisaz, The inhibitory effect of pyrophosphate on calcium oxalate precipitation and its relation to urolithiasis. *Experientia* **20**, 276–277 (1964).
24. L. Kovacevic, H. Lu, N. Kovacevic, Y. Lakshmanan, Effect of bisphosphonates on the crystallization of stone-forming salts in synthetic urine. *Investig. Clin. Urol.* **61**, 310–315 (2020).
25. Y. Nakagawa *et al.*, Urine glycoprotein crystal growth inhibitors. Evidence for a molecular abnormality in calcium oxalate nephrolithiasis. *J. Clin. Invest.* **76**, 1455–1462 (1985).
26. Y. Nakagawa, M. Ahmed, S. L. Hall, S. Deganello, F. L. Coe, Isolation from human calcium oxalate renal stones of nephrocalcin, a glycoprotein inhibitor of calcium oxalate crystal growth. Evidence that nephrocalcin from patients with calcium oxalate nephrolithiasis is deficient in gamma-carboxyglutamic acid. *J. Clin. Invest.* **79**, 1782–1787 (1987).
27. E. M. Worcester, Y. Nakagawa, C. L. Wabner, S. Kumar, F. L. Coe, Crystal adsorption and growth slowing by nephrocalcin, albumin, and tamm-horsfall protein. *Am. J. Physiol.* **255**, F1197–F1205 (1988).
28. J. Asplin, S. DeGanello, Y. N. Nakagawa, F. L. Coe, Evidence that nephrocalcin and urine inhibit nucleation of calcium oxalate monohydrate crystals. *Am. J. Physiol.* **261**, F824–F830 (1991).
29. B. Hess, Y. Nakagawa, J. H. Parks, F. L. Coe, Molecular abnormality of Tamm-Horsfall glycoprotein in calcium oxalate nephrolithiasis. *Am. J. Physiol.* **260**, F569–F578 (1991).
30. H. Shiraga *et al.*, Inhibition of calcium oxalate crystal growth in vitro by uropontin: Another member of the aspartic acid-rich protein superfamily. *Proc. Natl. Acad. Sci. U.S.A.* **89**, 426–430 (1992).
31. J. S. Gleberzon, Y. Liao, S. Mittler, H. A. Goldberg, B. Grohe, Incorporation of osteopontin peptide into kidney stone-related calcium oxalate monohydrate crystals: A quantitative study. *Urolithiasis* **47**, 425–440 (2019).
32. S. N. Pillay, J. R. Asplin, F. L. Coe, Evidence that calgranulin is produced by kidney cells and is an inhibitor of calcium oxalate crystallization. *Am. J. Physiol.* **275**, F255–F261 (1998).
33. K. Kohri *et al.*, Biomolecular mechanism of urinary stone formation involving osteopontin. *Urol. Res.* **40**, 623–637 (2012).
34. B. Hess, U. Meinhardt, L. Zipperle, R. Giovanoli, P. Jaeger, Simultaneous measurements of calcium oxalate crystal nucleation and aggregation: Impact of various modifiers. *Urol. Res.* **23**, 231–238 (1995).
35. C. Cerini *et al.*, Nucleation of calcium oxalate crystals by albumin: Involvement in the prevention of stone formation. *Kidney Int.* **55**, 1776–1786 (1999).
36. G. A. Rose, S. Sulaiman, Tamm-horsfall mucoproteins promote calcium oxalate crystal formation in urine: Quantitative studies. *J. Urol.* **127**, 177–179 (1982).
37. D. S. Scurr, W. G. Robertson, Modifiers of calcium oxalate crystallization found in urine. III. Studies on the role of Tamm-Horsfall mucoprotein and of ionic strength. *J. Urol.* **136**, 505–507 (1986).
38. A. Kletzmayr *et al.*, Inhibitors of calcium oxalate crystallization for the treatment of oxalate nephropathies. *Adv. Sci. (Weinh)* **7**, 1903337 (2020).
39. D. Kim *et al.*, Bio-inspired multifunctional disruptors of calcium oxalate crystallization. *Nat. Commun.* **16**, 5229 (2025).
40. T. Jung *et al.*, Probing crystallization of calcium oxalate monohydrate and the role of macromolecule additives with in situ atomic force microscopy. *Langmuir* **20**, 8587–8596 (2004).
41. S. Schultze-Lam, G. Harauz, T. J. Beveridge, Participation of a cyanobacterial S layer in fine-grain mineral formation. *J. Bacteriol.* **174**, 7971–7981 (1992).
42. S. Schultze-Lam, T. J. Beveridge, Nucleation of celestite and strontianite on a cyanobacterial S-layer. *Appl. Environ. Microbiol.* **60**, 447–453 (1994).
43. A. J. Giuffre, L. M. Hamm, N. Han, J. J. De Yoreo, P. M. Dove, Polysaccharide chemistry regulates kinetics of calcite nucleation through competition of interfacial energies. *Proc. Natl. Acad. Sci. U.S.A.* **110**, 9261–9266 (2013).

44. X. Li *et al.*, Spatial patterns of carbonate biomineralization in biofilms. *Appl. Environ. Microbiol.* **81**, 7403–7410 (2015).
45. X. Liu *et al.*, DNA framework-encoded mineralization of calcium phosphate. *Chem* **6**, 472–485 (2020).
46. D. N. Azulay, M. Fraenkel, L. Chai, A bacterial biofilm polysaccharide affects the morphology and structure of calcium oxalate crystals. *Crystal Growth Design* **23**, 7853–7862 (2023).
47. H.-S. Xu *et al.*, Survival and viability of nonculturable *Escherichia coli* and *Vibrio cholerae* in the estuarine and marine environment. *Microb. Ecol.* **8**, 313–323 (1982).
48. M. Relucenti *et al.*, Microscopy methods for biofilm imaging: Focus on SEM and VP-SEM pros and cons. *Biology (Basel)* **10**, 51 (2021).
49. V.-D. Hodoroaba, "Energy-dispersive X-ray spectroscopy (EDS)" in *Characterization of Nanoparticles, Micro and Nano Technologies*, V. -D. Hodoroaba, W. E. S. Unger, A. G. Shard, Eds. (Elsevier, 2020), pp. 397–417.
50. V. Lešer, D. Drobne, Ž Pipan, M. Milani, F. Tatti, Comparison of different preparation methods of biological samples for FIB milling and SEM investigation. *J. Microsc.* **233**, 309–319 (2009).
51. R. Flannigan, W. H. Choy, B. Chew, D. Lange, Renal struvite stones–Pathogenesis, microbiology, and management strategies. *Nat. Rev. Urol.* **11**, 333–341 (2014).
52. Y. M. Romanova *et al.*, Microbial communities on kidney stones. *Mol. Genet. Microbiol. Virol.* **30**, 78–84 (2015).
53. R. K. Flannigan *et al.*, Evaluating factors that dictate struvite stone composition: A multi-institutional clinical experience from the EDGE Research Consortium. *Can. Urol. Assoc. J.* **12**, 131–136 (2017).
54. N. A. Sutton, N. Hughes, P. S. Handley, A comparison of conventional SEM techniques, low temperature SEM and the electroscan wet scanning electron microscope to study the structure of a biofilm of Streptococcus crista CR3. *J. Appl. Bacteriol.* **76**, 448–454 (1994).
55. M. Bossù *et al.*, Characterization of Scardovia wiggsiae biofilm by original scanning electron microscopy protocol. *Microorganisms* **8**, 807 (2020).
56. J. H. Priester *et al.*, Enhanced visualization of microbial biofilms by staining and environmental scanning electron microscopy. *J. Microbiol. Methods* **68**, 577–587 (2007).
57. H.-C. Flemming, J. Wingender, The biofilm matrix. *Nat. Rev. Microbiol.* **8**, 623–633 (2010).
58. H. C. Srivastava, G. A. Adams, Constitutions of polysaccharides from *Serratia marcescens*. *Can. J. Chem.* **40**, 1415–1424 (1962).
59. M. S. Byrd *et al.*, Genetic and biochemical analyses of the *Pseudomonas aeruginosa* Psl exopolysaccharide reveal overlapping roles for polysaccharide synthesis enzymes in Psl and LPS production. *Mol. Microbiol.* **73**, 622–638 (2009).
60. C. Wan *et al.*, *Escherichia coli* exopolysaccharides disrupt *Pseudomonas aeruginosa* biofilm and increase its antibiotic susceptibility. *Acta Biomater.* **185**, 215–225 (2024).
61. B. L. Griffiths, S. Karlsson, C. P. C. Soh, A. B. S. J. Dawnay, D. M. Swallow, Tamm-Horsfall glycoprotein: A lectin binding study. *Glycoconj. J.* **1**, 183–190 (1984).
62. H. H. Reinhart, N. Obedeanu, J. D. Sobel, Quantitation of Thmm-Horsfall protein binding to uropathogenic Escherichia coli and lectins. *J. Infect. Dis.* **162**, 1335–1340 (1990).
63. M. Strathmann, J. Wingender, H.-C. Flemming, Application of fluorescently labelled lectins for the visualization and biochemical characterization of polysaccharides in biofilms of Pseudomonas aeruginosa. *J. Microbiol. Methods* **50**, 237–248 (2002).
64. M. Alhede *et al.*, Combination of microscopic techniques reveals a comprehensive visual impression of biofilm structure and composition. *FEMS Immunol. Med. Microbiol.* **65**, 335–342 (2012).
65. S. Thiberge *et al.*, Scanning electron microscopy of cells and tissues under fully hydrated conditions. *Proc. Natl. Acad. Sci. U.S.A.* **101**, 3346–3351 (2004).
66. T. Tsuda *et al.*, SEM observation of wet biological specimens pretreated with room-temperature ionic liquid. *Chembiochem* **12**, 2547–2550 (2011).
67. J. H. Luft, Electron microscopy of cell extraneous coats as revealed by ruthenium red staining. *J. Cell Biol.* **23**, 54A–55A (1964).
68. R. J. Marcus *et al.*, Biofilms in nephrology. *Expert Opin. Biol. Ther.* **8**, 1159–1166 (2008).
69. S. Guo, M. D. Ward, J. A. Wesson, Direct visualization of calcium oxalate monohydrate crystallization and dissolution with atomic force microscopy and the role of polymeric additives. *Langmuir* **18**, 4284–4291 (2002).
70. M. Sivaguru *et al.*, Geobiology reveals how human kidney stones dissolve in vivo. *Sci. Rep.* **8**, 13731 (2018).
71. M. Sivaguru, J. C. Lieske, A. E. Krambeck, B. W. Fouke, Geobiomed sheds new light on human kidney stone crystallization and dissolution. *Nat. Rev. Urol.* **17**, 1–2 (2020).
72. K. H. Nealson, D. Saffarini, Iron and manganese in anaerobic respiration: Environmental significance, physiology, and regulation. *Annu. Rev. Microbiol.* **48**, 311–343 (1994).
73. T. Hobbs, L. N. Schultz, E. G. Lauchnor, R. Gerlach, D. Lange, Evaluation of biofilm induced urinary infection stone formation in a novel laboratory model system. *J. Urol.* **199**, 178–185 (2018).
74. J. J. Saw *et al.*, In vivo entombment of bacteria and fungi during calcium oxalate, brushite, and struvite urolithiasis. *Kidney360* **2**, 298 (2021).
75. E. J. Espinosa-Ortiz, R. Gerlach, "Struvite stone formation by ureolytic biofilms" in *The Role of Bacteria in Urology*, D. Lange, K. B. Scotland, Eds. (Springer International Publishing, 2019), pp. 61–70.
76. D. C. Dominguez, Calcium signalling in bacteria. *Mol. Microbiol.* **54**, 291–297 (2004).
77. I. Kolodkin-Gal, M. R. Parsek, M. A. Patrauchan, The roles of calcium signaling and calcium deposition in microbial multicellularity. *Trends Microbiol.* **31**, 1225–1237 (2023).
78. G. S. Manning, Limiting laws and counterion condensation in polyelectrolyte solutions I. Colligative properties. *J. Chem. Phys.* **51**, 924–933 (1969).
79. X. Qiu *et al.*, Measuring inter-DNA potentials in solution. *Phys. Rev. Lett.* **96**, 138101 (2006).
80. X. Qiu *et al.*, Inter-DNA attraction mediated by divalent counterions. *Phys. Rev. Lett.* **99**, 038104 (2007).
81. G. C. L. Wong, L. Pollack, Electrostatics of strongly charged biological polymers: Ion-mediated interactions and self-organization in nucleic acids and proteins. *Annu. Rev. Phys. Chem.* **61**, 171–189 (2010).
82. A. R. Ferrão *et al.*, Quantification of ions in human urine–A review for clinical laboratories. *Biomedicines* **12**, 1848 (2024).
83. S. J. Cole, A. R. Records, M. W. Orr, S. B. Linden, V. T. Lee, Catheter-associated urinary tract infection by *Pseudomonas aeruginosa* is mediated by exopolysaccharide-independent biofilms. *Infect. Immun.* **82**, 2048–2058 (2014).
84. W. H. Boyce, F. K. Garvey, The amount and nature of the organic matrix in urinary calculi: A review. *J. Urol.* **76**, 213–227 (1956), 10.1016/S0022-5347(17)66686-2.
85. H. Liang, T. E. Angelini, J. Ho, P. V. Braun, G. C. L. Wong, Molecular imprinting of biomineralized CdS nanostructures: Crystallographic control using self-assembled DNA—membrane templates. *J. Am. Chem. Soc.* **125**, 11786–11787 (2003).
86. H. Liang, T. E. Angelini, P. V. Braun, G. C. L. Wong, Roles of anionic and cationic template components in biomineralization of CdS nanorods using self-assembled DNA—membrane complexes. *J. Am. Chem. Soc.* **126**, 14157–14165 (2004).
87. J. A. Wesson, M. D. Ward, Pathological biomineralization of kidney stones. *Elements* **3**, 415–421 (2007).
88. J. A. Wesson, Comparison of calcium oxalate stone matrix proteomics data to predictions from in vitro studies of protein-crystal interactions. *Crystal Growth Design* **25**, 452–461 (2025).
89. L. E. Muñoz *et al.*, Neutrophil extracellular traps initiate gallstone formation. *Immunity* **51**, 443–450.e4 (2019).
90. Z. Yang *et al.*, Neutrophil extracellular traps drive kidney stone formation. *Kidney Dis. (Basel)* **11**, 11–24 (2024).
91. M. Allesen-Holm *et al.*, A characterization of DNA release in *Pseudomonas aeruginosa* cultures and biofilms. *Mol. Microbiol.* **59**, 1114–1128 (2006).
92. L. Montanaro *et al.*, Extracellular DNA in biofilms. *Int. J. Artif. Organs* **34**, 824–831 (2011).
93. A. M. T. Barnes, K. S. Ballering, R. S. Leibman, C. L. Wells, G. M. Dunny, *Enterococcus faecalis* produces abundant extracellular structures containing DNA in the absence of cell lysis during early biofilm formation. *mBio* **3**, e00193-12 (2012).
94. C. B. Whitchurch, T. Tolker-Nielsen, P. C. Ragas, J. S. Mattick, Extracellular DNA required for bacterial biofilm formation. *Science* **295**, 1487–1487 (2002).
95. E. S. Gloag *et al.*, Self-organization of bacterial biofilms is facilitated by extracellular DNA. *Proc. Natl. Acad. Sci. U.S.A.* **110**, 11541–11546 (2013).
96. S. Farmanesh *et al.*, Natural promoters of calcium oxalate monohydrate crystallization. *J. Am. Chem. Soc.* **136**, 12648–12657 (2014).
97. J. D. Rimer *et al.*, Crystal growth inhibitors for the prevention of l-cystine kidney stones through molecular design. *Science* **330**, 337–341 (2010).
98. A. G. Shtukenberg *et al.*, Dislocation-actuated growth and inhibition of hexagonal l-cystine crystallization at the molecular level. *Crystal Growth Design* **15**, 921–934 (2015).
99. L. N. Poloni *et al.*, Role of molecular recognition in l-cystine crystal growth inhibition. *Crystal Growth Design* **17**, 2767–2781 (2017).
100. K. Yoshimura *et al.*, Emergency drainage for urosepsis associated with upper urinary tract calculi. *J. Urol.* **173**, 458–462 (2005).
101. A. K. T. Kirschner, J. Vierheilig, H.-C. Flemming, J. Wingender, A. H. Farnleitner, How dead is dead? Viable but non-culturable versus persister cells. *Environ. Microbiol. Rep.* **13**, 243–245 (2021).
102. M. S. Pearle *et al.*, Medical management of kidney stones: AUA guideline. *J. Urol.* **192**, 316–324 (2014).
103. C. Sahli *et al.*, Recent advances in nanotechnology for eradicating bacterial biofilm. *Theranostics* **12**, 2383–2405 (2022).
104. W. C. Schmidt, Data for "Intercalated bacterial biofilms are intrinsic internal components of calcium-based kidney stones." Figshare. Available at https://doi.org/10.6084/m9.figshare.31014964. Deposited 6 January 2026.